2017

Accuracy consideration by DRP schemes for DNS and LES of compressible flow computations

Björn Sjögreen
NASA Ames Research Center, Bjorn.Sjogreen@multid.se

Helen C. Yee
NASA Ames Research Center, yee@nas.nasa.gov

Computers and Fluids 159 (2017) 123–136

Contents lists available at ScienceDirect

Computers and Fluids

journal homepage: www.elsevier.com/locate/compfluid

Accuracy consideration by DRP schemes for DNS and LES of compressible flow computations☆

Björn Sjögreen, H.C. Yee*

NASA Ames Research Center, USA

ARTICLE INFO

Article history:
Received 16 March 2017
Revised 8 August 2017
Accepted 21 September 2017
Available online 28 September 2017

Keywords:
High order nonlinear filter schemes
DRP schemes
DNS & LES computations

ABSTRACT

Several dispersion relation-preserving (DRP) spatially central discretizations are considered as the base scheme in the framework of the Yee & Sjögreen low dissipative nonlinear filter approach. In addition, the nonlinear filter of Yee & Sjögreen with shock-capturing and long time integration capabilities is used to replace the standard DRP linear filter for both smooth flows and flows containing discontinuities. DRP schemes for computational aeroacoustics (CAA) focus on dispersion error consideration for long time linear wave propagation rather than the formal order of accuracy of the scheme. The resulting DRP schemes usually have wider grid stencils and increased CPU operations count compared with standard central schemes of the same formal order of accuracy. For discontinuous initial data and long time wave propagation of smooth acoustic waves, various space and time DRP linear filter are needed. For acoustic waves interacting with shocks and turbulence induced noise, DRP schemes with linear filters alone usually are not capable of simulating such flows. The investigation presented in this paper is focused on the possible gain in efficiency and accuracy by spatial DRP schemes over standard central schemes having the same grid stencil width for general direct numerical simulations (DNS) and large eddy simulations (LES) of compressible flows. Representative test cases for both smooth flows and problems containing discontinuities for 3D DNS of compressible gas dynamics are included.

Published by Elsevier Ltd.

1. Introduction

The construction of stable and accurate numerical methods for long time integration of complex multiscale compressible shock-free turbulent flows, turbulent flows containing discontinuities, steep gradients, and vortical flows share some common requirements with dispersion relation-preserving (DRP) schemes (optimized low-dispersion schemes) for computational aeroacoustics (CAA) [5,8,27,28]. The design criteria for accurate and stable methods for such applications are very different from those for shorter time integration of non-turbulence/non-acoustic unsteady flows and rapidly developing shock-wave interaction simulations. Standard direct numerical simulations (DNS) and large eddy simulations (LES) usually require high accuracy schemes in terms of low dissipative and low dispersive errors in space and time. It is common to have numerically induced high frequency oscillations (spurious numerical artifacts) due to long time integration of non-dissipative or low-dissipative finite discretizations. A good numerical method for DNS and LES should be able to minimize these spurious oscillations while at the same maintaining stability and accuracy during an entire long-time evolution. Unlike many DNS and LES numerical considerations, the amplitude of acoustic waves is similar to that of numerical noise. A good CAA method should be able to distinguish the two. This paper only addresses the spatial discretization by the method-of-lines approach. Controlling low dissipative and low dispersive temporal errors is important but outside the scope of this investigation. Highly accurate appropriate temporal discretizations and, when appropriate, with small time steps are assumed to be used in conjunction with the current development

Here, the term "DRP" schemes has been used loosely, according to the recent definition of DRP methods by Tam [27], to include general schemes that perform various optimizations to reduce numerical dispersion errors for different applications. Most CAA related DRP methods employed techniques to minimize dispersion error to resolve linear acoustic waves over long distances without compromising the real physical behavior of the wave form propagation of the initial boundary value problem (IBVP). A large percentage of DRP methods utilized least squares, L_1-norm, L_2-norm, L_∞-norm, and other integral metrics to minimize the numerical

☆ Special issue in Computers & Fluids in honor of Prof. Eleuterio F. Toro's 70th birthday, 2017.

* Corresponding author.
E-mail addresses: bjorn.sjogreen@multid.se (B. Sjögreen), Helen.M.Yee@nasa.gov (H.C. Yee).

https://doi.org/10.1016/j.compfluid.2017.09.017
0045-7930/Published by Elsevier Ltd.

wavenumber error over prescribed intervals in order to obtain the grid stencil coefficients. The resulting DRP schemes usually have wider grid stencil than their standard central schemes of the same order of accuracy. Low dispersive temporal discretization and special treatments for IBVPs of the different CAA applications are also needed. See Tam [27,28], Brambley [5], and Haras & Taasan [8] and Linders & Nordström and Linders et al. [15,16] for formulations and overviews. Some of the DRP schemes might perform poorly for decaying or growing oscillations. See Brambley [5] for a study. For discontinuous initial data and long time wave propagations of smooth acoustics waves, various space and time DRP linear filters are needed. For acoustics waves interacting with shocks and turbulence induced noise, DRP schemes with linear filters alone usually are not capable of simulating such flows.

According to Tam [27], optimized compact schemes are also DRP schemes. For over 20 years high order compact spatial discretizations in conjunction with linear high order compact filters have been methods of choice for many DNS and LES of incompressible and low speed compressible turbulent/acoustic flows due to their advantage of requiring a very low number of grid points per wavelength and flexibility in geometry handling. However, most optimized compact schemes were not designed for long-time integration and additional constraints are needed. See Haras & Taasan [8] for the construction of compact finite difference schemes for long time integration. In addition, the advantage of compact schemes seems to require additional investigation and research for compressible turbulent flows containing moderate and strong shock waves. One popular method is by employing a blending of high order compact spatial schemes with high order shock-capturing schemes. Another more efficient approach for turbulence with discontinuities is the nonlinear filter approach of Yee et al., Yee & Sjögreen and Sjögreen & Yee [20,31,36]. They employed the high order compact scheme as their spatial base scheme. The Yee & Sjögreen studies [33] indicated that for shock-wave turbulence interactions the accuracy performance of compact schemes is similar to the central scheme of the same order under the Yee & Sjögreen nonlinear filter approach.

The Yee & Sjögreen [32] adaptive nonlinear filter method consists of a high order non-dissipative spatial base scheme and a nonlinear filter step. The nonlinear filter step consists of a flow sensor and the dissipative portion of a high resolution high order shock-capturing method to guide the application of the shock-capturing dissipation where needed. The nonlinear filter idea was first initiated by Yee et al. [36] using an artificial compression method of Harten [9] as the flow sensor. Smart flow sensors were developed at a later stage by the same investigators and collaborators in [13,14,20,20,31]. The smart flow sensor provides the locations and the estimated strength of the necessary numerical dissipation needed at these locations and leaves the rest of the flow field free of shock-capturing dissipations. It is noted that the nonlinear filter approach of Yee & Sjögreen [32] requires one Riemann solver per time step per grid point for each spatial direction. It is independent of the time discretization to be used. However, hybrid schemes (switching between high order non-dissipative methods and high order shock-capturing methods) would require four Riemann solvers per time step per grid point for each spatial direction if a fourth-stage Runge–Kutta time discretization is used. Unlike the hybrid method, our highly parallelizable adaptive nonlinear filter schemes do not rely on switching between schemes to avoid the related numerical instability and conservation consideration at switching locations. These nonlinear filter scheme with adaptive numerical dissipation control in high order shock-capturing schemes and their hybrid cousins have shown excellent performance for certain turbulent test cases. For more practical 3D test cases of DNS and LES of compressible shock-free turbulence, low speed turbulence with shocklets, and supersonic turbulence for non-periodic boundaries in curvilinear geometries, some improvement in numerical stability is needed without resorting to added numerical dissipation that can interfere with the accuracy of numerical simulations.

Starting in the early 80s, skew-symmetric splitting of certain components of the inviscid flux derivatives in conjunction with central schemes was shown to help with numerical stability for long time integration. For certain splittings they can provide a stable energy norm estimate for the Euler equations with smooth flows. For other skew-symmetric formulations they can provide a discrete momentum conservation or a discrete kinetic preservation property. See Arakawa, Blaisdell et al., Yee et al., Yee & Sjögreen, Sjögreen & Yee and Kotov et al. [1,2,6,13,14,21,31,32,35] for some discussions and performance of the combined approach for DNS and LES applications. A semi-conservative skew-symmetric splitting (entropy splitting) of Yee et al. [35] in conjunction with the nonlinear filter approach to improve numerical stability without added ad hoc numerical dissipation was conducted in 2000. It has been utilized extensively in DNS of shock-free turbulence. See [26] and their later work for their wide applications. For the present study for test cases governed by nonlinear conservation laws, (especially with discontinuities), Ducros et al. skew-symmetric splitting [6] is also part of the Yee & Sjögreen [32] nonlinear filter scheme approach for DRP spatial base scheme operations. Note that some of the skew-symmetric splitting for the gas dynamics flux derivatives are not applicable and/or cannot be straightforwardly extended to the ideal MHD [35]. Their construction is also dependent on the MHD governing equation formulation. For their skew-symmetric splitting extension to the ideal MHD, see Sjögreen & Yee and Sjögreen et al. [22,23].

This paper only considers several DRP central spatial schemes as the base scheme in the framework of the Yee & Sjögreen[32] low dissipative nonlinear filter method approach. DRP time discretizations are not considered. For time discretization we utilize the low dissipative fourth-order Runge–Kutta method with small time steps for the investigation to minimize dispersion error due to time discretizations. The investigation is focused on the possible gain in accuracy by DRP schemes over the standard central schemes of the same grid stencil for general DNS and LES compressible flow computations. As mentioned before, CAA focuses on dispersion error consideration for long time linear wave propagation rather than the formal order of accuracy of the scheme. The resulting DRP schemes usually have wider grid stencil and increase in CPU operations count than their standard central schemes of the same order of accuracy. For discontinuous initial data and long time wave propagations of smooth acoustics waves various space and time DRP linear filters are needed. For acoustics waves interacting with shocks and turbulence induced noise DRP schemes with linear filters alone usually are not capable of simulating such flows. Due to this fact, here, the Yee & Sjögreen nonlinear filter step with shock-capturing and long time integration properties is to replace the spatial DRP linear filter. To show the performance of our current approach, representative test cases for smooth flows, problems containing discontinuities and 3D DNS computations for the compressible gas dynamics are included.

2. Ducros et al. conservative splitting

Standard centered difference approximations of nonlinear conservation laws normally encounter nonlinear instabilities after a short time integration without added numerical dissipation. It is well known that the appearance of these instabilities can be delayed if the convective flux derivatives are written in an equivalent desired split form before the pure central approximation is employed. Hereafter this is referred to as a split approximation.

For nonlinear systems, such as the Euler equations of gas dynamics, split approximations have been used for a long time; see, e.g., Ducros et al. and Blaisdell et al. [2,6]. A split approximation starts from rewriting the derivative of the product $(ab)_x$ as

$$\frac{1}{2}(ab)_x + \frac{1}{2}(a)_x b + \frac{1}{2}a(b)_x, \tag{1}$$

and this split form is approximated by,

$$\frac{1}{2}D(ab) + \frac{1}{2}D(a)b + \frac{1}{2}aD(b), \tag{2}$$

where D is a finite difference operator, and a and b are functions of x.

As shown in Ducros et al. [6], the approximation (2) can be written in conservation form. For example, with the second-order operator $Du_j = (u_{j+1} - u_{j-1})/(2\Delta x)$, it holds that

$$\frac{1}{2}D(ab) + \frac{1}{2}D(a)b + \frac{1}{2}aD(b) = \frac{1}{4\Delta x}\Delta_+[(a_j + a_{j-1})(b_j + b_{j-1})], \tag{3}$$

where $\Delta_+ q_j = (q_{j+1} - q_j)$.

Eq. (3) can be generalized to arbitrary $2p+1$ point wide antisymmetric operators

$$D_p u_j = \frac{1}{\Delta x}\sum_{k=1}^{p}\alpha_k(u_{j+k} - u_{j-k}) \tag{4}$$

For example, standard centered difference operators of pth-order of accuracy are of this form with coefficients $\alpha_k = \alpha_k^{(p)}$ determined by the order conditions

$$\sum_{k=1}^{p} k\alpha_k^{(p)} = \frac{1}{2} \qquad \sum_{k=1}^{p}\alpha_k^{(p)}k^{2n+1} = 0, \quad n = 1, \ldots, p-1. \tag{5}$$

To derive the conservative form of the split approximation for an arbitrary operator, the right hand side of the algebraic identity

$$\begin{aligned} &a_{j+k}b_{j+k} - a_{j-k}b_{j-k} + (a_{j+k} - a_{j-k})b_j + a_j(b_{j+k} - b_{j-k}) \\ &\quad = (a_{j+k} + a_j)(b_{j+k} + b_j) - (a_j + a_{j-k})(b_j + b_{j-k}) \end{aligned} \tag{6}$$

is written on conservative form by

$$\begin{aligned} &(a_{j+k} + a_j)(b_{j+k} + b_j) - (a_j + a_{j-k})(b_j + b_{j-k}) \\ &\quad = \sum_{m=0}^{k-1}(a_{j-m} + a_{j+k-m})(b_{j-m} + b_{j+k-m}) \\ &\qquad - \sum_{m=0}^{k-1}(a_{j-1-m} + a_{j-1+k-m})(b_{j-1-m} + b_{j-1+k-m}) \end{aligned} \tag{7}$$

The conservative form of the split approximation becomes

$$\begin{aligned} &\frac{1}{2}D_p(ab) + \frac{1}{2}D_p(a)b + \frac{1}{2}aD_p(b) = \frac{1}{\Delta x}\sum_{k=1}^{p}\frac{1}{2}\alpha_k\big((a_{j+k}b_{j+k} \\ &- a_{j-k}b_{j-k}) + a_j(b_{j+k} - b_{j-k}) + (a_{j+k} - a_{j-k})b_j\big) = \frac{1}{\Delta x}\sum_{k=1}^{p}\frac{\alpha_k}{2} \\ &\times\left(\sum_{m=0}^{k-1}(a_{j-m} + a_{j+k-m})(b_{j-m} + b_{j+k-m}) - \sum_{m=0}^{k-1}(a_{j-1-m} \right. \\ &\left. + a_{j-1+k-m})(b_{j-1-m} + b_{j-1+k-m})\right) = \frac{1}{\Delta x}(h_{j+1/2} - h_{j-1/2}) \end{aligned} \tag{8}$$

where the numerical flux is defined by

$$h_{j+1/2} = \sum_{k=1}^{p}\frac{1}{2}\alpha_k\sum_{m=0}^{k-1}(a_{j-m} + a_{j+k-m})(b_{j-m} + b_{j+k-m}) \tag{9}$$

For the three dimensional gas dynamics equations the inviscid flux in the x-direction flux is

$$\mathbf{f} = ([\rho u, \rho u^2 + p, \rho uv, \rho uw, (e+p)u]^T,$$

where ρ denotes density, u, v, w are velocities in the x-, y-, and z-directions, p is the pressure, and e is the total energy. The flux components can be written as products of two factors in many different ways, leading to different split approximations. The Ducros et al. split approximation of the gas dynamics flux derivative that will be used in this study is given by

$$\mathbf{f}_x|_{x=x_j} \approx \begin{pmatrix} \frac{1}{2}D\rho_j u_j + \frac{1}{2}\rho_j Du_j + \frac{1}{2}u_j D\rho_j \\ \frac{1}{2}D\rho_j u_j^2 + \frac{1}{2}\rho_j u_j Du_j + \frac{1}{2}u_j D\rho_j u_j + Dp_j \\ \frac{1}{2}D\rho_j u_j v_j + \frac{1}{2}\rho_j v_j Du_j + \frac{1}{2}u_j D\rho_j v_j \\ \frac{1}{2}D\rho_j u_j w_j + \frac{1}{2}\rho_j w_j Du_j + \frac{1}{2}u_j D\rho_j w_j \\ \frac{1}{2}Du_j(e_j + p_j) + \frac{1}{2}u_j D(e_j + p_j) + \frac{1}{2}(e_j + p_j)Du_j \end{pmatrix}. \tag{10}$$

which by (9) can be written on conservative form with numerical flux function

$$\begin{aligned} \mathbf{h}_{j+1/2} = &\frac{1}{2}\sum_{k=1}^{p}\alpha_k\sum_{m=1}^{k-1} \\ &\times\begin{pmatrix} (\rho_{j-m} + \rho_{j+k-m})(u_{j-m} + u_{j+k-m}) \\ (\rho_{j-m}u_{j-m} + \rho_{j+k-m}u_{j+k-m}) \\ (u_{j-m} + u_{j+k-m}) + p_{j-m} + p_{j+k-m} \\ (\rho_{j-m}v_{j-m} + \rho_{j+k-m}v_{j+k-m})(u_{j-m} + u_{j+k-m}) \\ (\rho_{j-m}w_{j-m} + \rho_{j+k-m}w_{j+k-m})(u_{j-m} + u_{j+k-m}) \\ (e_{j-m} + p_{j-m} + e_{j+k-m} + p_{j+k-m}) \\ (u_{j-m} + u_{j+k-m}) \end{pmatrix} \end{aligned} \tag{11}$$

3. DRP schemes

Since our objective is to utilize wave number optimized schemes for general DNS and LES applications, no attempt is made to obtain optimized schemes for specific IBVPs with specific initial data and boundary data. In this study three different optimized finite difference operators are considered. See Tam [27] and De Roeck et al. [18] for the development and references cited therein. These are: (a) DRP4S7, the original Tam & Webb fourth-order accurate DRP operator with a seven-point wide grid stencil, (b) DRP4S9, the fourth-order accurate DRP operator with a nine-point wide grid stencil, and (c) STO9, the fourth-order accurate operator with a nine-point wide stencil by Bogey & Bailly [3]. All three operators have antisymmetric coefficients and are optimized over wave number intervals $0 \le k\Delta x \le 1.1$ for DRP4S7 and $\pi/16 \le k\Delta x \le \pi/2$ for DRP4S9 and STO9. Here Δx is the grid spacing and the integer k is the mode number. DRP4S7 and STO9 were studied in [18].

Remark. Numerical experiments made with DRP4S7 optimized over $\pi/16 \le k\Delta x \le \pi/2$ gave worse accuracy than with DRP4S7 optimized over the more standard choice $0 \le k\Delta x \le 1.1$ used here. It is reasonable to expect that with fewer free parameters, the interval of optimization would be made shorter.

DRP4S7 and DRP4S9 use least square minimization of the absolute error, i.e., integral over the square of the error in wave number space. The STO9 scheme uses L_1 optimization of the relative error in wave number space, i.e., integral over the absolute value of the error divided by $k\Delta x$, since $k\Delta x$ is the exact wave number.

Their difference operators D for the first-order derivative of a grid function u_j are of the form

$$Du_j = \frac{1}{h}\sum_{k=1}^{q}a_k(u_{j+k} - u_{j-k}). \tag{12}$$

Table 1 gives the coefficients of the DRP4S7 scheme, Table 2 lists the coefficients of the DRP4S9 scheme, and Table 3 shows the coefficients of the STO9 scheme. The STO9 coefficients were obtained

Table 1
Coefficients of DRP4S7, optimized over [0, 1.1].

k	a_k
1	0.77088238051822552
2	−0.16670590441458047
3	0.02084314277031176

Table 2
Coefficients of DRP4S9, optimized over $[\pi/16, \pi/2]$.

k	a_k
1	0.846863763009931
2	−0.251240526849904
3	0.063181723773749
4	−0.008481970157843

Table 3
Coefficients of STO9, optimized over $[\pi/16, \pi/2]$, from [18].

k	a_k
1	0.841570216389881
2	−0.244678789340406
3	0.059463699920073
4	−0.007650934367322

from [18], where they are given with 12 decimals. In this work we extended the number of decimals by enforcing the fourth order accuracy constraint to high precision.

Note that the centered operators (12) are of the same anti-symmetric form as (4). This means that the Ducros et al. splitting described in Section 2 is also straightforwardly applicable to be used for these optimized operators described in this section.

4. Classical central and DRP as base schemes with skew-symmetric splitting as preprocessing step in the framework of the nonlinear filter method of Yee & Sjögreen [32]

This section gives a brief overview of the high-order nonlinear filter scheme of Yee et al. and Yee & Sjögreen [31,32,34,35] for accurate computations of DNS and LES of compressible turbulence for a wide range of flow types by introducing as little shock-capturing numerical dissipation as possible. For simplicity, the discussion uses the 3D inviscid Euler equation.

Preprocessing Step by Skew-symmetric Splitting for Gas Dynamics: Before the application of a high-order non-dissipative spatial base scheme, a preprocessing step is employed to improve numerical stability. The inviscid flux derivatives of the governing equations are split into the following two ways, depending on the flow types and the desire for rigorous mathematical analysis or physical argument.

- Entropy splitting of [35] or the natural splitting described in previous section: These are non-conservative splittings and they are among some of the best in improving numerical stability for non-dissipative central schemes, especially for long time integration of shock-free turbulence.
- The Ducros et al. splitting [6] for systems (or variants of the conservative skew-symmetric splitting described earlier): These are conservative splittings and are suitable for problems with discontinuities.

Remark. For problems containing discontinuities, conservative skew-symmetric splittings should be used.

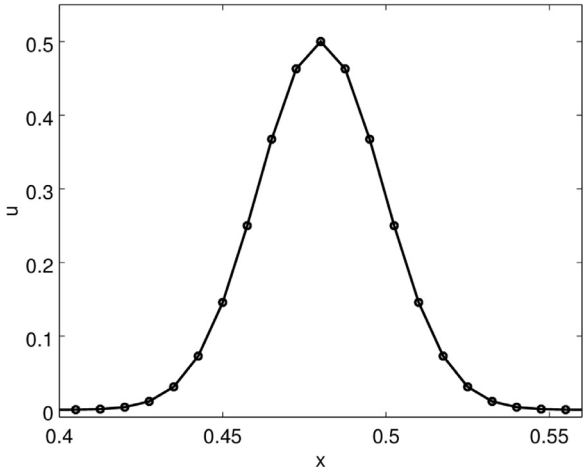

Fig. 1. Smooth initial data of the linear advection problem.

Base Scheme Step after the Preprocessing Step: A full time step is advanced using a high-order non-dissipative (or very low dissipation) spatially central scheme on the split form of the governing partial differential equations (PDEs) (i.e., after the preprocessing step). For the current study fourth-order to eighth-order classical central schemes and the three DRP4S7, DRP4S9 and STO9 DRP schemes are considered as base schemes. Only results by eighth-order central scheme are shown in the numerical experiment section.

For the base scheme step a full time step of high-order temporal discretization such as the fourth-order Runge–Kutta (RK4) method is used. It is remarked that other DRP temporal discretizations can be used for the base scheme step. See Tam [27,28], Brambley [5], and Haras & Taasan [8].

Post-Processing (Nonlinear Filter Step): To further improve the accuracy of the computed solution from the base scheme step, after a full time step of a non-dissipative high-order spatial base scheme on the split form of the governing equation(s), the post-processing step is used to nonlinearly filter the solution by a dissipative portion of a high-order shock-capturing scheme with a local flow sensor. Comparable order of accuracy of the nonlinear filter dissipation with the base scheme usually is considered. For non-entropy satisfying shock-capturing schemes it is assumed that entropy satisfying fixes for both 1D and multi-D are employed [37]. For extreme flows positivity-preserving shock-capturing schemes should be used. See Kotov et al. [11,12] for some performance of positivity-preserving nonlinear filter schemes.

The flow sensor provides locations and amounts of built-in shock-capturing dissipation that can be further reduced or eliminated. At each grid point a local flow sensor is employed to analyze the regularity of the computed flow data. Only the strong discontinuity locations would receive the full amount of shock-capturing dissipation. In smooth regions no shock-capturing dissipation would be added unless high frequency oscillations develop, owning to the possibility of numerical instability in long time integrations of nonlinear governing PDEs. In regions with strong turbulence, if needed, a small fraction of the shock-capturing dissipation would be added to improve stability.

Note that the filter numerical fluxes only involve the inviscid flux derivatives, regardless if the flow is viscous or inviscid. If viscous terms are present, a matching high order central difference operator (as the inviscid difference operator) is included on the base scheme step. For ease of summation-by-parts numerical boundary closure implementation for the viscous flux derivatives, the same inviscid central difference operator for the first derivative is employed twice for the viscous flux derivatives.

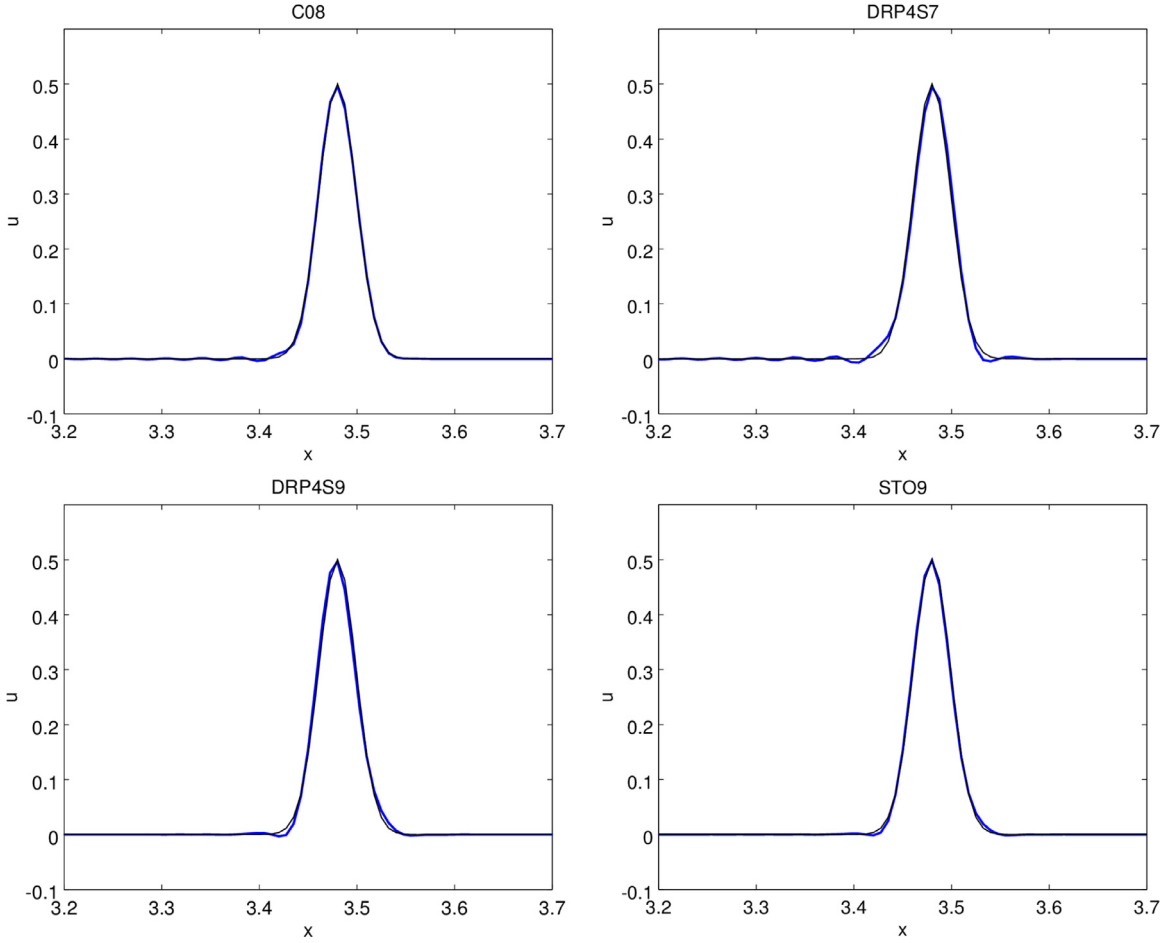

Fig. 2. Gaussian pulse: C08 (left top) and optimized schemes without any linear or nonlinear filter, DRP4S7 (right top), DRP4S9 (right bottom), and STO9 (left bottom). Solutions at $t = 3$ of the linear advection problem. Computed solution plotted in blue color, exact solution shown in black color. (For interpretation of the references to color in this figure legend, the reader is referred to the web version of this article.)

Remark. For gas dynamics the post-processing (nonlinear filter step) is employed for all of the equations for both non-reacting and reacting flows. For the MHD on a uniform Cartesian grid, in order to obtain zero discrete div **B** error without any div **B** cleaning, the nonlinear filter step is not employed for the three magnetic field equations. See Yee & Sjögreen [34] for details.

For simplicity of presentation, considered the 3D Euler equations

$$\frac{\partial U}{\partial t} + \frac{\partial E}{\partial x} + \frac{\partial F}{\partial y} + \frac{\partial G}{\partial z} = 0, \tag{13}$$

where E, F and G are inviscid in the x, y and z directions, respectively.

Let U^* be the solution after the completion of the full time step of the base scheme step. The final update of the solution after the filter step is (with the numerical fluxes in the y- and z-directions as well as their corresponding y- and z-direction indices on the x inviscid flux omitted)

$$U^{n+1}_{j,k,l} = U^*_{j,k,l} - \frac{\Delta t}{\Delta x}[H^*_{j+1/2} - H^*_{j-1/2}], \quad H^*_{j+1/2} = R_{j+1/2}\overline{H}_{j+1/2}, \tag{14}$$

where $R_{j+1/2}$ is the matrix of right eigenvectors of the Jacobian of the inviscid flux vector in terms of Roe's average states based on U^*. $H^*_{j+1/2}$ and $H^*_{j-1/2}$ are "filter" numerical fluxes in terms of Roe's average states based on U^*. Denote the elements of the filter numerical flux vector $\overline{H}_{j+1/2}$ by $\overline{h}^l_{j+1/2}$, $l = 1, 2, \ldots, 5$, where $\overline{h}^l_{j+1/2}$ has the form

$$\overline{h}^l_{j+1/2} = \frac{\kappa^l_{j+1/2}}{2} w^l_{j+1/2} \phi^l_{j+1/2}. \tag{15}$$

Here $w^l_{j+1/2}$ is a flow sensor to activate the nonlinear numerical dissipation portion of a high order shock-capturing scheme $\frac{1}{2}\phi^l_{j+1/2}$, and $\kappa^l_{j+1/2}$ is a positive flow dependent parameter that is less than or equal to one to control the amount of shock-capturing dissipation to be used. The nonlinear dissipative portion of a high-resolution shock-capturing scheme "$\frac{1}{2}\phi^l_{j+1/2}$" can be any shock-capturing scheme. The choice of the parameter $\kappa^l_{j+1/2}$ can be different for different flow types and is automatically chosen by using the local $\kappa^l_{j+1/2}$ described in [32]. The flow sensor $w^l_{j+1/2}$ can be a variety of formulae introduced in the literature or can be switched from one flow sensor to another, depending on the computed flow data at that particular location. For a variety of local flow sensors with automatic selection of the proper parameter, depending on different flow type, see [32]. The form of Tauber–Sandham [30] for the filter numerical flux uses the Ducros et al. flow sensor [7] as $\kappa^l_{j+1/2}$ and the Harten artificial compression method formula (ACM) [9] as the flow sensor indicated in [36] and similarly in [17] is part of the Yee & Sjögreen adaptive numerical dissipation control generalization filter formulae. For the numerical experiments presented, we mainly concentrate on the wavelet flow sensor of Yee & Sjögreen, the Ducros et al. flow sensor [7] and the artificial compression method flow sensor of [36]. For the wavelets

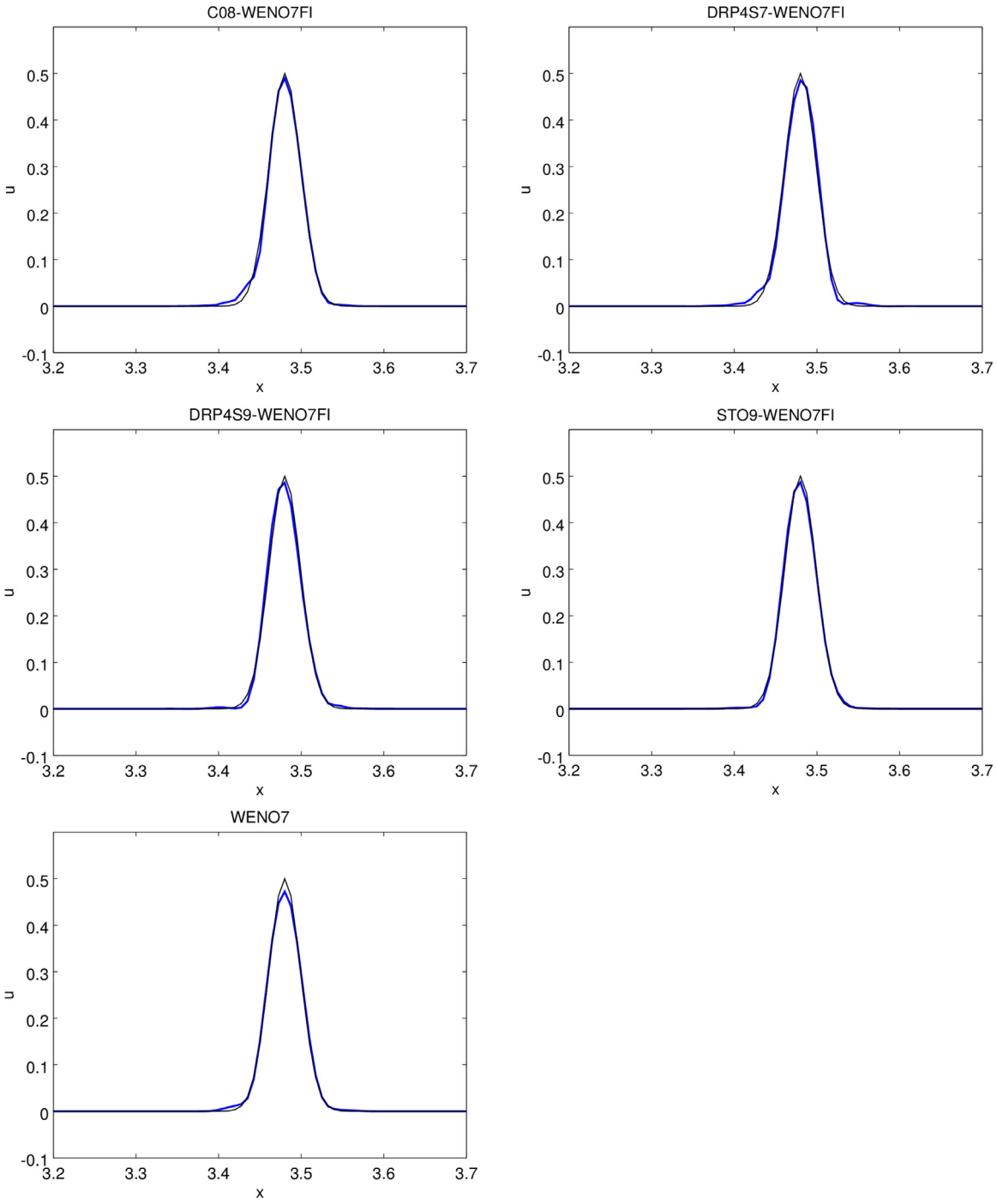

Fig. 3. Gussian pulse: Standard nonlinear filter scheme C08+WENO7fi (left top). Optimized nonlinear filter schemes, DRP4S7+WENO7fi (right top), DRP4S9+WENO7fi (middle left), STO9+WENO7fi (middle right), and standard shock-capturing scheme WENO7 (left bottom). Solutions at time $t = 3$ of the linear advection problem. Computed solution plotted in blue color, exact solution shown in black color. (For interpretation of the references to color in this figure legend, the reader is referred to the web version of this article.)

and ACM flow sensors, see the aforementioned references cited. The Ducros et al. flow sensor was designed mainly to capture flows containing shocks and vorticity with the *divcurl* tolerance of the form

$$sw = \frac{(\nabla \cdot \mathbf{u})^2}{(\nabla \cdot \mathbf{u})^2 + \omega^2 + \varepsilon}. \tag{16}$$

Here $\mathbf{u}$ is the velocity vector, ω is the vorticity magnitude and ε is a small number to avoid division by zero (e.g., 10^{-6}). The Ducros et al. flow sensor consists of a cut off parameter δ as an input parameter based on the value of *sw* that can be used to switch on or off the dissipative portion of the high order shock-capturing scheme. If δ is set to be one, the dissipation only switches on when it encounters a shock wave. For a lower value of the cut off δ parameter, vorticity can be detected. The δ parameter is used as the $\kappa^i_{j+1/2}$ for the Durcros et al. flow sensor.

The low Mach number κ curve was developed in Yee & Sjögreen [32] and detail is omitted here. Local flow sensors for a wide spectrum of flow speed and shock strength developed in [13,14,32] are also omitted here.

The aforementioned high order nonlinear filter method is valid for the four forms of the MHD formulation and the four skew-

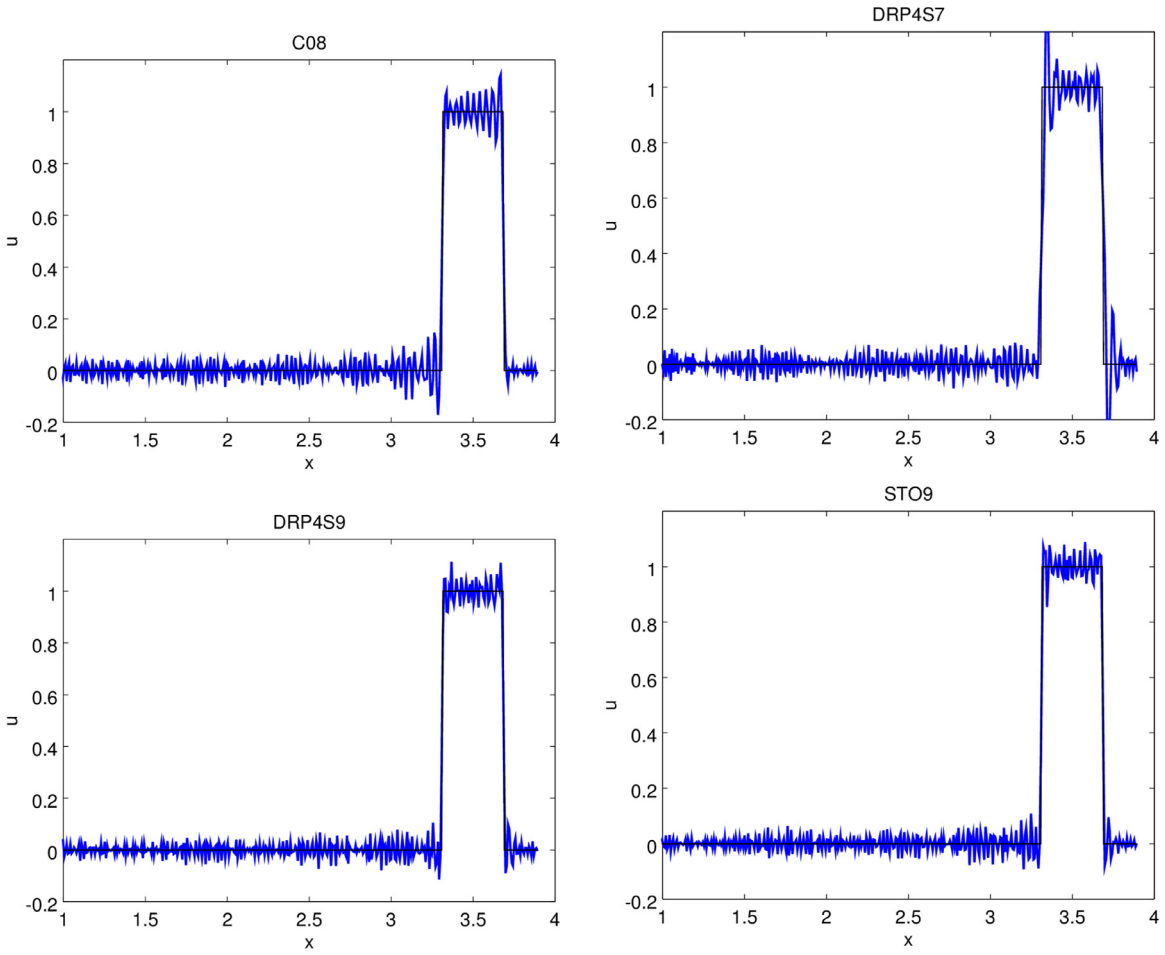

Fig. 4. Square pulse: C08 (left top). Optimized schemes without linear or nonlinear filter, DRP4S7 (right top), DRP4S9 (left bottom), and STO9 (bottom right). Solutions at $t = 3$ of the linear advection problem with square pulse initial data. Computed solution plotted in blue color, exact solution shown in black color. (For interpretation of the references to color in this figure legend, the reader is referred to the web version of this article.)

symmetric splittings of the MHD to be used as the preprocessing step. In addition, the aforementioned high order nonlinear filter method is valid for the four forms of the MHD formulation and the different high order entropy conservative numerical fluxes, such as the spatial base schemes discussed in Sections 4 and 5 of Sjögreen & Yee [24,25].

From here on, without loss of generality, the term "a split scheme" refers to the use of a high order central scheme to discretize a skew-symmetric splitting form of the inviscid flux derivatives. If the three considered DRP4S7, DRP4S9 and STO9 schemes are used as the base schemes, and the dissipative portion of the seventh-order WENO (WENO7) is used as the nonlinear filter, they are denoted by DRP4S7+WENO7fi, DRP4S9+WENO7fi, and STO9+WENO7fi respectively. Similarly if WENO5fi is used, they are denoted by DRP4S7+WENO5fi, DRP4S9+WENO5fi, and STO9+WENO5fi. If an eighth-order classical central difference operator is used as the base scheme for the aforementioned three DRP schemes, it is denoted by C08+WENO7fi. If Ducros et al.splitting is used, e.g., it is denoted by C08-DS+WENO7fi.

5. Numerical results

This section shows numerical results for five test cases for the compressible gas dynamics. The test cases include problems with smooth flows, problems containing shock waves, shock-free turbulence and turbulence with weak shocks. These test cases are well known test cases in the literature and will be used to illustrate the performance of the proposed methods. The first three test cases are commonly used simple 1D and 2D test cases as a prelude to turbulent computations. The last two test cases are 3D DNS computations of the Taylor-Green vortex and isotropic turbulence. They are included to show that our proposed schemes are suitable for DNS of turbulent flows.

Here, for illustration purposes, only two smart flow sensors (among the many variants indicated in [32] and Kotov et al. [13,14]) are chosen for the numerical experiment for the nonlinear filter approach. Except for the DNS test cases, the third-order B-spline wavelet flow sensor developed in Sjögreen & Yee [20] was employed. For the DNS computations the Ducros et al. flow sensor was employed. This is due to the fact that the Ducros et al. flow sensor is most suited for these two particular DNS computations. See Kotov et al. [13,14] for the studies.

5.1. Scalar linear wave results

In this subsection the scalar advection equation

$$u_t + u_x = 0 \quad t \geq 0 \tag{17}$$

is solved on an interval $0 \leq x \leq 3.9$ with periodic boundary condition. Initial data will be either a Gaussian pulse or a square pulse. The domain and initial data are scaled such that the problem is equivalent with the linear advection problem solved in [18]. It is noted that Ducros et al. splitting is not applicable for linear equations. In addition, the Ducros et al. flow sensor is only applicable for higher than 1D nonlinear Euler/Navier-Stokes equations.

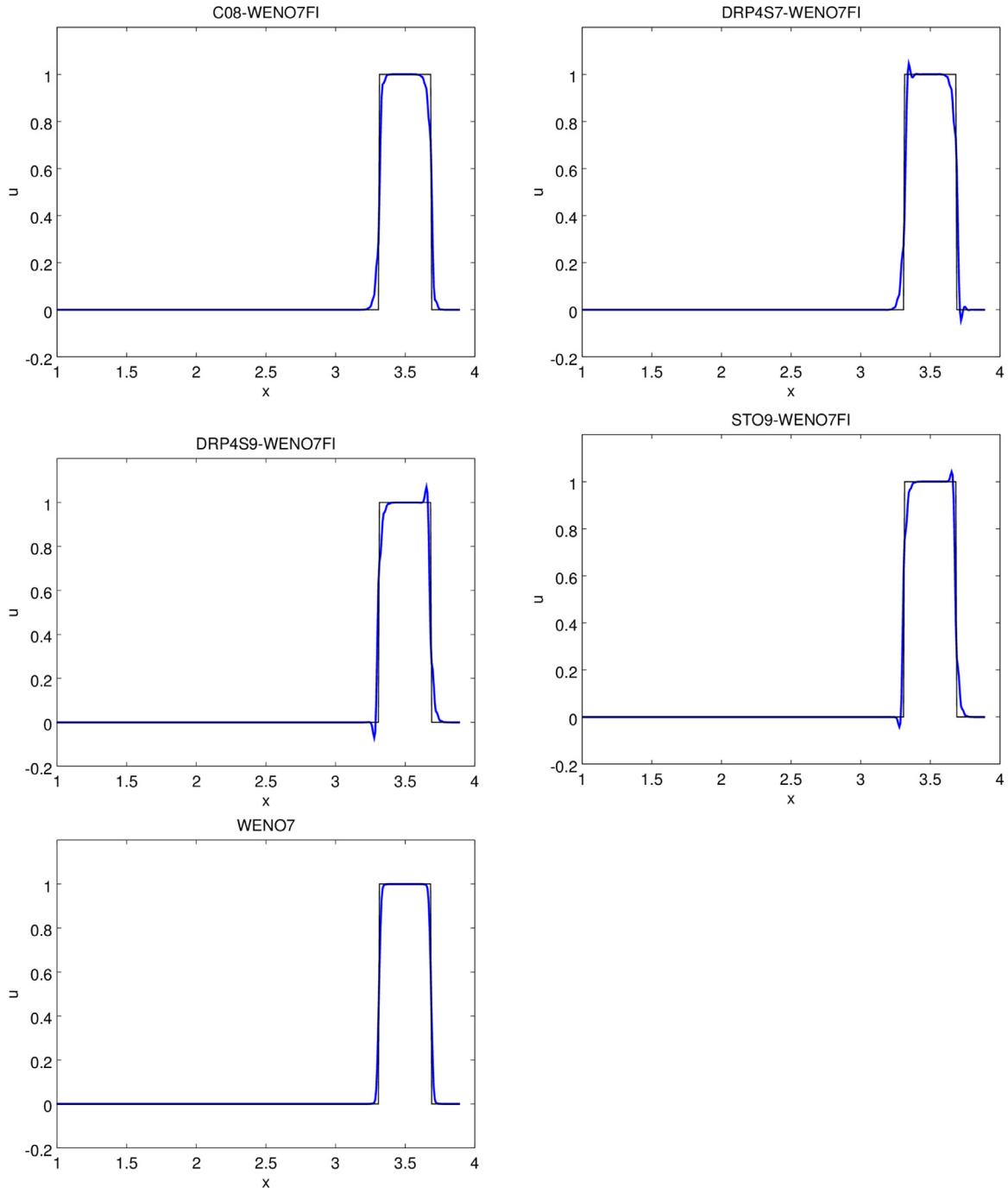

Fig. 5. Square pulse: Standard nonlinear filter scheme C08+WEBO7fi (left top). Optimized nonlinear filter schemes, DRP4S7+WENO7fi (right top), DRP4S9+WENO7fi (left middle), STO9+WENO7fi (right middle), and standard shock-capturing scheme WENO7 (left bottom). Solutions at $t = 3$ of the linear advection problem with square pulse initial data. Computed solution plotted in blue color, exact solution shown in black color. (For interpretation of the references to color in this figure legend, the reader is referred to the web version of this article.)

5.1.1. Smooth initial data: Gaussian pulse

The advection Eq. (17) is solved with initial data

$$u(x,0) = \frac{1}{2} e^{-K(x-x_c)^2},$$

where $K = 1369.2$ and $x_c = 0.48$. The spatial discretization has 520 grid points, the CFL number is 0.1, and the problem is solved to time $t = 3$, which since the wave speed is 1, means that the pulse has traveled 3 length units. Fig. 1 shows a close up of the initial data near x_c. The pulse is resolved with approximately 15 grid points. Computed results are displayed in Figs. 2 and 3. The nine-point stencil optimized nonlinear filter schemes, DRP4S9+WENO7fi and STO9+WENO7fi, appear to be more accurate than the other methods, especially on the lower left side of the pulse. The dissipative nature of the WENO7 scheme is also visible as a somewhat lower peak value than the other methods.

5.1.2. Discontinuous initial data: Square pulse

The advection Eq. (17) is solved with initial data

$$u(x,0) = \begin{cases} 1 & 0.3124 \le x < 0.6875 \\ 0 & otherwise \end{cases}.$$

Also for this initial data, the spatial discretization has 520 grid

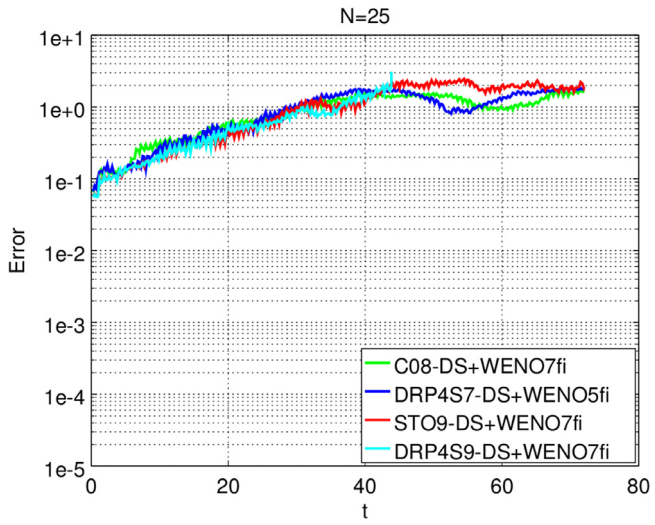

Fig. 6. Compressible 2D Euler equations. Vortex convection on a uniform grid with 25^2 points. Norm of error vs. time for C08-DS+WENO7fi, DRP4S7-DS+WENO5fi, DRP4S9-DS+WENO7fi, and STO9-DS+WENO7fi. (For interpretation of the references to color in this figure legend, the reader is referred to the web version of this article.)

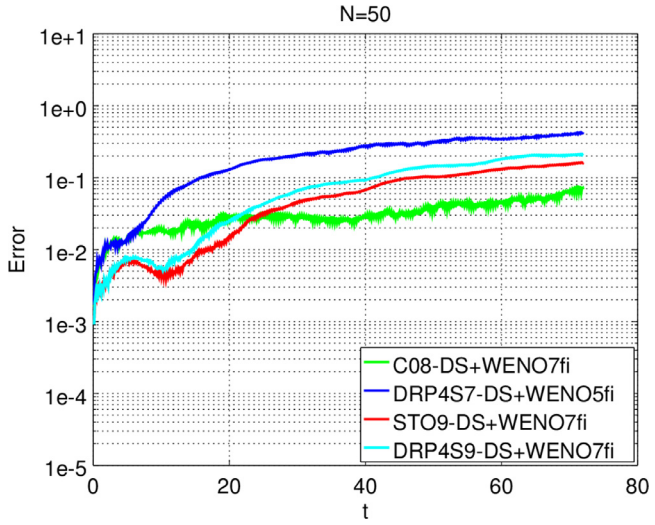

Fig. 7. Compressible 2D Euler equations. Vortex convection on a grid with 50^2 points. Norm of error vs. time for C08-DS+WENO7fi, DRP4S7-DS+WENO5fi, DRP4S9-DS+WENO7fi, and STO9-DS+WENO7fi.

points, the CFL number is 0.1, and the problem is solved to time 3. Computed results are displayed in Figs. 4 and 5. The C08, DRP4S7, DRP4S9 and STO9 without nonlinear filter exhibit oscillatory solutions. With linear filters and DRP time discretization indicated in [18,27], the oscillations are suppressed. See [18] for the result. Here, the nonlinear filter version of the DRP methods are

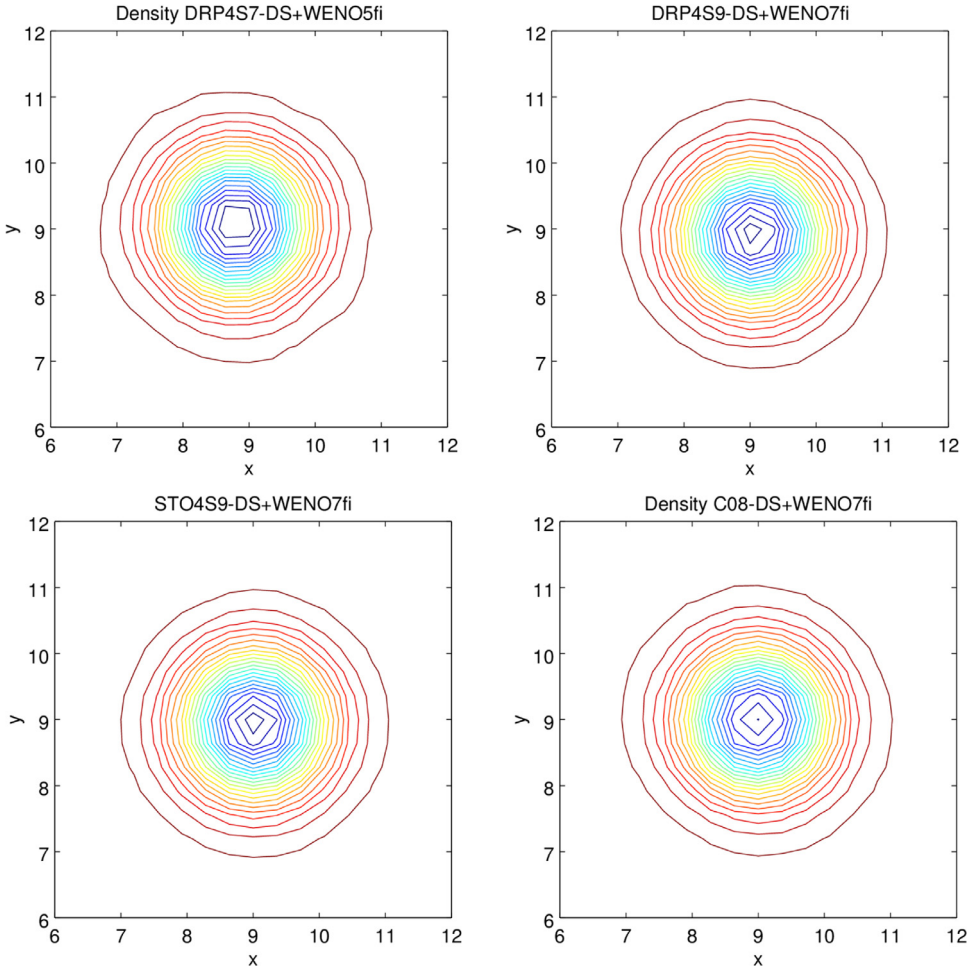

Fig. 8. Compressible 2D Euler equations. Density contour lines at the final time (t=72) on a grid with 50^2 grid points. Upper left DRP4S7-DS+WENO5fi, upper right DRP4S9-DS+WENO7fi, lower left STO9-DS+WENO7fi, and lower right C08-DS+WENO7fi.

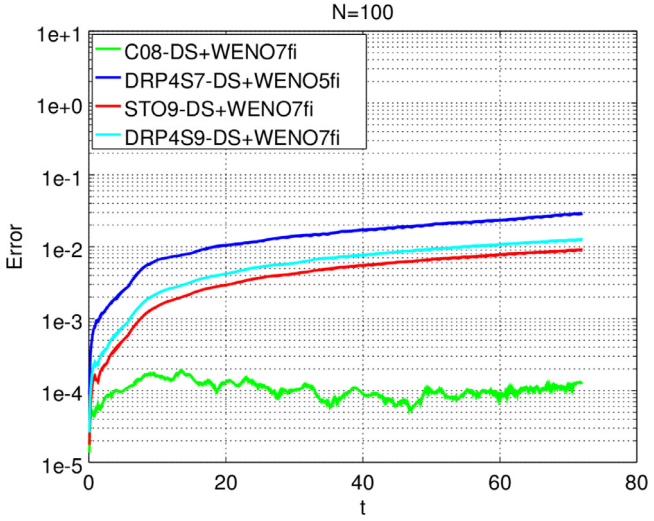

Fig. 9. Compressible 2D Euler equations. Vortex convection on a grid with 100^2 points. Norm of error vs. time for C08-DS+WENO7fi, DRP4S7-DS+WENO5fi, DRP4S9-DS+WENO7fi, and STO9-DS+WENO7fi.

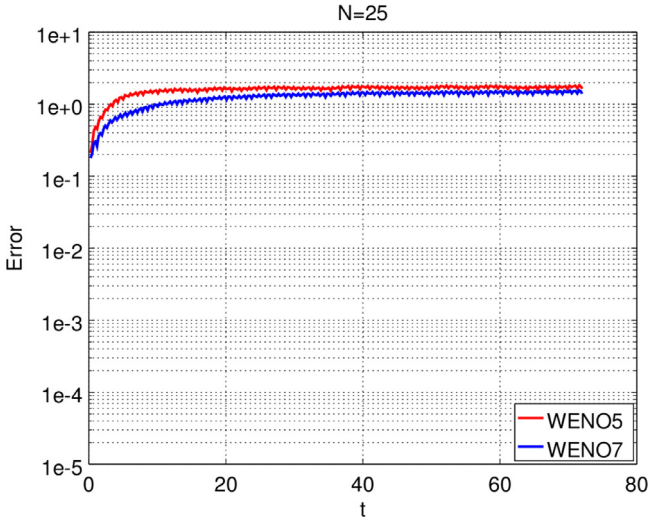

Fig. 10. Compressible 2D Euler equations. Vortex convection on a uniform grid with 25^2 points. Norm of error vs. time for WENO5 (red) and WENO7 (blue). (For interpretation of the references to color in this figure legend, the reader is referred to the web version of this article.)

able to suppress some of the oscillations. However, the WENO7 scheme, which is designed for discontinuous solutions, shows the best performance. The optimized nine-point stencil nonlinear filter methods agree somewhat better with the exact solution, especially near the 'corners' of the pulse, than DRP4S7+WENO7fi and C08+WENO7fi.

5.2. 2D Compressible euler simulation of smooth flow: Isentropic vortex convection

The compressible Euler equations in two space dimensions are solved with initial data

$$\rho(x,y) = \left(1 - \frac{(\gamma-1)\beta^2}{8\gamma\pi^2} e^{1-r^2}\right)^{\frac{1}{\gamma-1}} \tag{18}$$

$$u(x,y) = u_\infty - \frac{\beta(y-y_0)}{2\pi} e^{(1-r^2)/2} \tag{19}$$

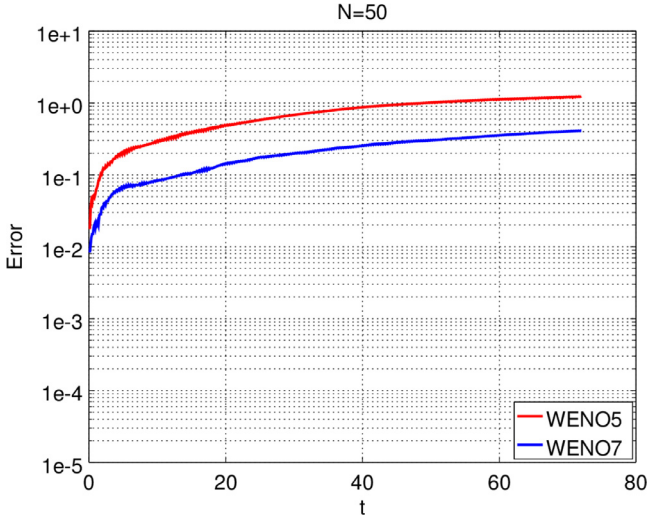

Fig. 11. Compressible 2D Euler equations. Vortex convection on a grid with 50^2 points. Norm of error vs. time for WENO5 (red) and WENO7 (blue). (For interpretation of the references to color in this figure legend, the reader is referred to the web version of this article.)

$$v(x,y) = v_\infty + \frac{\beta(x-x_0)}{2\pi} e^{(1-r^2)/2} \tag{20}$$

$$p(x,y) = \rho(x,y)^\gamma, \tag{21}$$

where $r^2 = x^2 + y^2$, $\beta = 5$, $\gamma = 1.4$, $u_\infty = 1$, and $v_\infty = 0$. The exact solution is the initial data translated, $\mathbf{u}(x,t) = \mathbf{u}_0(x - u_\infty t, y - v_\infty t)$.

The computational domain was of size $0 \le x \le 18$, $0 \le y \le 18$ with periodic boundary conditions. The center of the vortex is chosen to be $(x_0, y_0) = (9, 9)$. The problem is solved in time with a fourth order accurate explicit Runge–Kutta method to time $t = 72$, which corresponds to four revolutions of the vortex across the domain.

All four methods were implemented on the split form described in Section 2.

The problem was solved with three different grid resolutions. The coarsest grid has 25×25 grid points, which gives approximately six grid points across the vortex. Fig. 6 shows the time evolution of the maximum norm of the error over all five equation components on this grid, for the different methods. The color coding in the plots is as follows: C08-DS+WENO7fi (green), DRP4S7-DS+WENO7fi (blue), STO9-DS+WENO7fi (red), and DRP4S9-DS+WENO7fi (cyan). Up to time $t = 40$ the four methods produce similar results and are hard to distinguish. At later times DRP4S7-DS+WENO5fi and C08-DS+WENO7fi have a smaller error than the nine-point optimized schemes. On this coarse grid DRP4S9+WENO7fi breaks down with negative density at time $t = 45$. This is the only combination of resolution and scheme that did not run the full four periods.

Fig. 7 shows the evolution of the norm of the error of density computed on a grid with 50×50 points. Here the two nine-point optimized schemes have smallest error up to time $t = 20$. It can be conjectured that this is the resolution at which the stencil optimization is effective. Fig. 8 compares the density of the vortex at the final time, $t = 72$, for the four different schemes. DRP4S7-DS+WENO5fi can be seen to have somewhat distorted shape, while the other three methods (DRP4S9-DS+WENO7fi, STO9-DS-WENO7fi, C08-DS-WENO7fi) show comparable density contour plots.

At the higher resolution 100×100 grid points, shown in Fig. 9, the higher order C08-DS+WENO7fi scheme is superior. In the limit

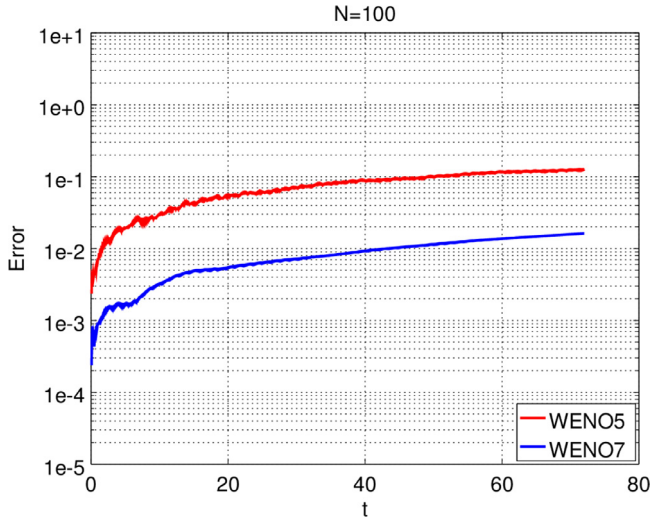

Fig. 12. Compressible 2D Euler equations. Vortex convection on a grid with 100^2 points. Norm of error vs. time for WENO5 (red) and WENO7 (blue). (For interpretation of the references to color in this figure legend, the reader is referred to the web version of this article.)

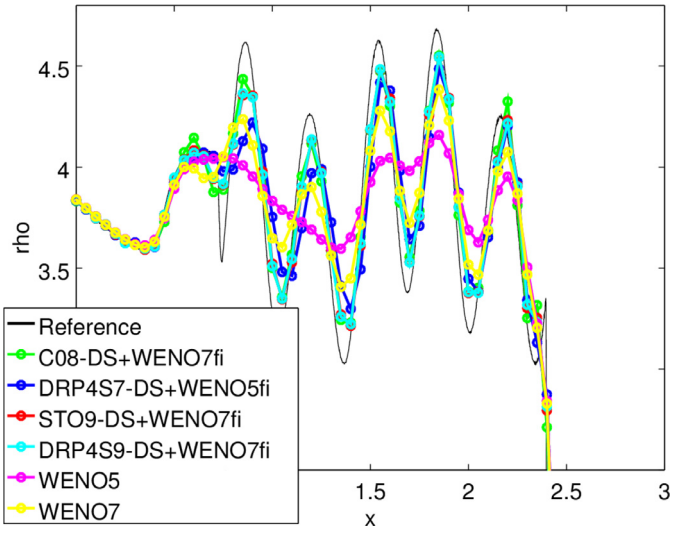

Fig. 13. 1D Osher-Shu test case. Close up of the density at time 1.8 for C08-DS+WENO7fi, DRP4S7-DS+WENO5fi, DRP4S9-DS+WENO7fi, STO9-DS+WENO7fi, WENO5, and WENO7 using a grid with 201 points.

of increased resolution it is reasonable to expect the schemes of highest formal order of accuracy to have the smallest actual errors.

The errors on the same grids, but computed by WENO5 and WENO7 are shown in Figs. 10, 11, –12. Here WENO5 is shown in red and WENO7 in blue. Note that Figs. 11–12 have one order of magnitude larger upper limit on the y-axis than the corresponding low dissipative results in Figs. 7–9.

5.3. 1D Compressible euler test case with shocks: Shu-Osher problem

The Shu-Osher problem [19] is a one-dimensional Mach 3 shock moving into an oscillatory density. A highly oscillatory flow field (1D turbulent flow) develops behind the shock wave. The problem is defined for the one dimensional Euler equations with $\gamma = 1.4$ and initial data

$$(\rho,\ u,\ p) = \begin{cases} (3.857143,\ 2.629369,\ 10.33333), & x < -4 \\ (1 + 0.2\sin 5x,\ 0,\ 1), & x \geq 4 \end{cases} \quad (22)$$

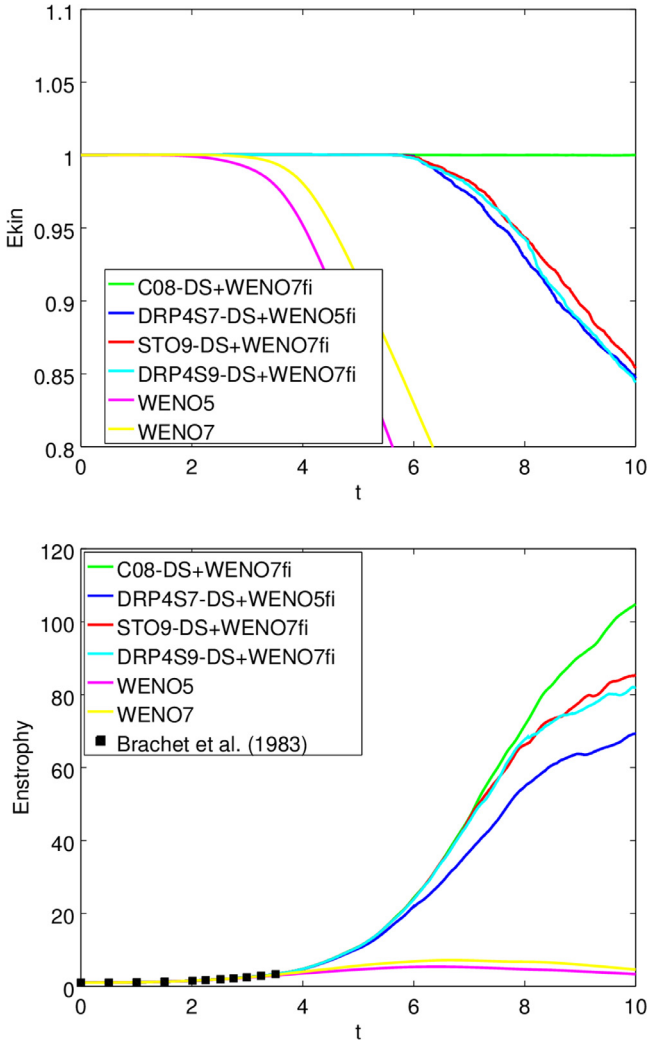

Fig. 14. 3D Compressible Euler equations. Taylor–Green vortex test case. Total kinetic energy vs. time (top) and enstrophy vs. time (bottom) for six different methods.

on the domain $-5 \leq x \leq 5$. The grid has 201 points, corresponding to discretization size $\Delta x = 0.05$. The nonlinear numerical dissipation is multiplied with sensors designed to activate it only in the neighborhood of shocks. In the computations shown here a wavelet sensor was used with two wavelet levels and a cut-off smoothness exponent 0.5.

Fig. 13 shows the density at the final time computed by the optimized stencil schemes DRP4S7, DRP4S9, and STO9, implemented in the Ducros et al. split form of the equations. The seventh order WENO dissipation is used as postprocessing filter (DRP4S7-DS+WENO7fi, DRP4S9-DS+WENO7fi, STO9-DS+WENO7fi). Also shown in the figure is the solution by the standard centered eight order nine-point scheme, with Ducros et al. splitting and WENO7 filter (C08-DS+WENO7fi). The computed densities by STO9-DS+WENO7fi and DRP4S9-DS+WENO7fi are very close. STO9-DS+WENO7fi, plotted in red color, is almost completely covered by the cyan colored DRP4S9-DS+WENO7fi.

For comparison, Fig. 13 also includes the solution obtained by the Jiang & Shu WENO5 and WENO7 schemes. Except for DRP4S7-DS+WENO5fi, the filter scheme captures the physical oscillations well on this very coarse grid. The resolution at the highly oscillatory part of Fig. 13 can be seen to be approximately 6 points per wavelength. Accuracy compares very favorably with the results by the WENO7 scheme. Higher accuracy can be obtained with a lo-

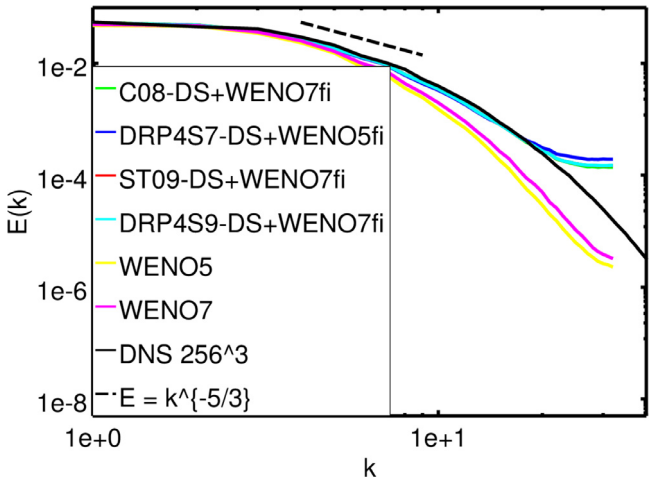

Fig. 15. 3D Isotropic turbulence test case. Energy spectra at the final time by six schemes using 64^3 grid points. DNS using 256^3 grid points also shown for comparison.

cal smart flow sensor in the use of the Yee & Sjögreen nonlinear filter scheme. Here we only show one global flow sensor for the computation.

See [24,25] for results on the same problem, but using entropy conserving base schemes instead of split schemes together with the WENO7 filter. Results in [24,25] with eighth-order accurate entropy conserving scheme have similar resolution of the post-shock oscillations as obtained here with C08-DS+WENO7fi. One advantage of split schemes is their computational cost is in general lower than the cost of entropy conserving schemes.

5.4. 3D Compressible euler shock-Free turbulence test case: Taylor–Green vortex

The Taylor–Green vortex [29] is a well-known shock-free compressible turbulence test problem that has been studied extensively. Extensive scheme comparison is reported in Kotov et al. [13] for DNS and LES simulations with grid refinement studies employing the high order central nonlinear filter scheme using the Ducros et al. splitting. The 3D Euler equations of compressible gas dynamics are solved with $\gamma = 5/3$. The computational domain is a cube with sides of length 2π and with periodic boundary conditions in all three directions. The initial data are

$$\rho = 1 \quad p = 100 + \{(\cos(2z) + 2)(\cos(2x) + \cos(2y)) - 2\}/16 \tag{23}$$

$$u = \sin x \cos y \cos z, \quad v = -\cos x \sin y \cos z, \quad w = 0. \tag{24}$$

The problem is solved to time 10 on a uniform grid with 64^3 grid points.

The total kinetic energy of the exact solution is constant in time. Fig. 14 shows the evolution of the total kinetic energy for the four different nonlinear filter schemes. All four methods conserve the kinetic energy extremely well. As the flow evolves, smaller scales are created, which causes an increase in the enstrophy. The enstrophy increase for the four different schemes can be seen in the right subplot of Fig. 14. These computed results agree well with the filter DNS using a 256^3 grid reported in [14] and the Brachet et al. [4] linearized theory (up to time $T < 4$). The results by WENO5 and WENO7, which perform poorly, are also included for comparison.

Remark: For this nearly incompressible low speed test case the schemes of choice in the literature are spectral and high order compact or central schemes with summation-by-parts boundary closures in conjunction with their respective high order linear filters. The nonlinear filter step is not needed. This study is to show the versatility of the proposed approach when a priori knowledge of the flow structure is not known, and/or for flows with a time varying random forcing and a wide range of flow speed regimes during the entire time-accurate evolution. See the Appendix of Kotov et al. for an illustration [14].

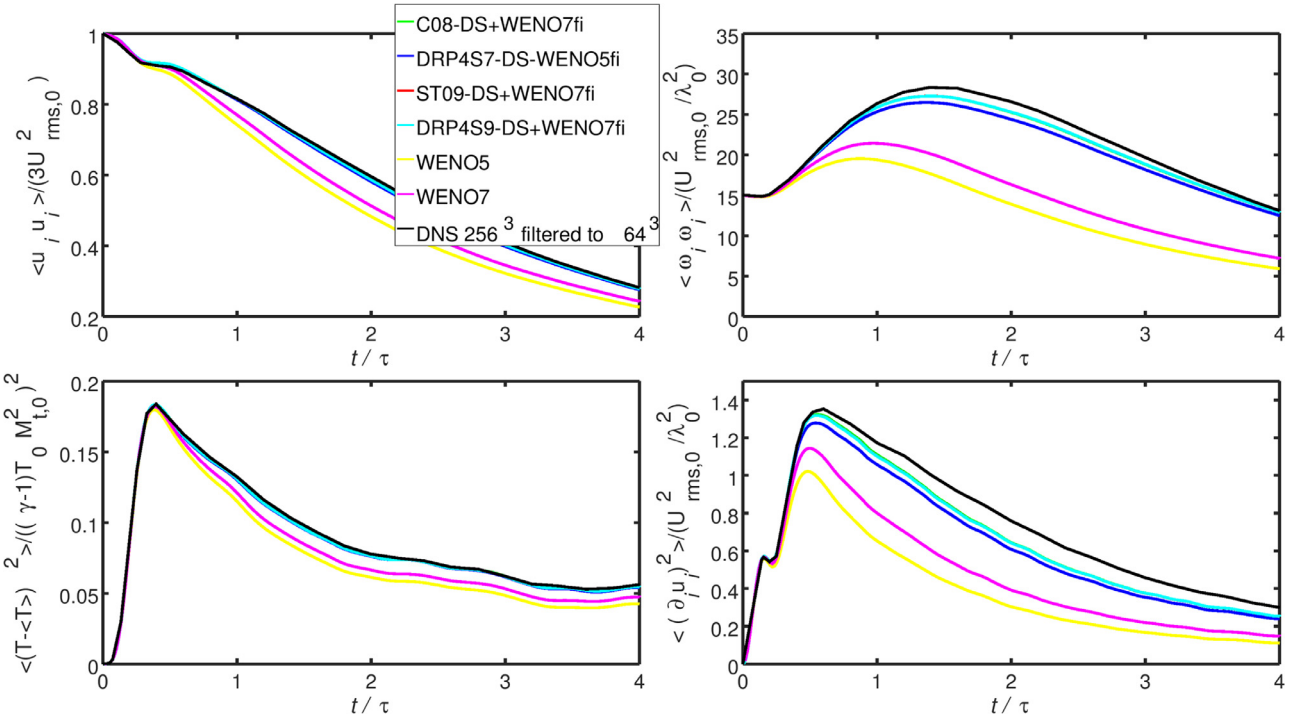

Fig. 16. 3D Isotropic turbulence test case. Evolution of kinetic energy (upper left), enstrophy (upper right), temperature variance (lower left), and dilatation (lower right), computed by six schemes, using 64^3 grid points. DNS using 256^3 grid points is also shown for comparison.

5.5. 3D Compressible euler turbulence with shocklets test case: Isotropic turbulence with eddy shocklets

This test case is a decaying compressible isotropic turbulence with eddy shocklets. For high enough turbulent Mach numbers weak shocks (shocklets) develop from the turbulent motion. In this test the initial turbulent Mach number is 0.6. The equations are solved using $\gamma = 1.4$. The computational domain is a cube with side length 2π and with periodic boundary conditions in all three directions. The initial datum is a random divergence free velocity field, $u_{i,0}$, $i = 1, 2, 3,$ that satisfies

$$\frac{3}{2}u_{rms,0}^2 = \frac{1}{2}\langle u_{i,0}, u_{i,0}\rangle = \int_0^\infty E(k)\,dk$$

with energy spectrum

$$E(k) \sim k^4 e^{-2(k/k_0)^2}.$$

The computations below were made with $u_{rms,0} = 1$ and $k_0 = 4$. The angular brackets denote averaging over the entire computational domain. The density and pressure fields are constant initially. See [13] for definitions of the quantities and more details about the set up of the problem. The simulation is run to the final time $t = 4$.

Fig. 15 compares the energy spectra by four nonlinear filter methods. Spectra by WENO5 and WENO7 are also shown. Fig. 16 shows the evolution in time of kinetic energy, enstrophy, temperature variation, and dilatation for the same schemes. In Figs. 15 and 16, the results with C08+WENO7fi, STO9+WENO7fi, and DRP4S9+WENOfi are indistiguishable, and the cyan colored curve (which was plotted last) covers the green and red curves. The results show agreement between the central base scheme and the optimized (DRP,STO) base schemes. These computed results agree well with the filtered DNS using a 256^3 grid reported in [14]. Performance of DNS and LES by WENO5 and WENO7 using the same 64^3 coarse grid is also reported in [14]. WENO5 and WENO7 results are more diffusive than the results obtained by nonlinear filter methods.

6. Conclusions

The Yee & Sjögreen and Kotov et al. [13,14,32] high order numerical method with the Ducros et al. skew-symmetric type of splitting for compressible gas dynamics has been extensively investigated for long time wave propagation of smooth flows, DNS of shock-free turbulence, and DNS of turbulence with weak, moderate and strong shocks, including forced turbulent flows.

This work combines DRP centered difference schemes, optimized for aeroacoustics, with numerical techniques developed for compressible fluid flows with shocks and small scale features. Specifically, DRP schemes are applied to the Ducros et al. split form of the compressible fluid equations, and the solution is post processed after each time step with dissipative portion of high-resolution shock-capturing methods with smart flow sensor to control the amount of numerical dissipation where needed.

The method is evaluated on standard test problems in compressible fluid dynamics, long time isentropic vortex convection, Taylor-Green vortex, shock/turbulence interaction and isotropic turbulence with shock waves. Numerical experiments demonstrated that DRP schemes and standard central schemes of the same grid stencil width in the framework of Yee & Sjögreen nonlinear filter approach are with almost similar accuracy on these types of test problem, as long as the grid resolution is not extremely high. Their CPU operations count for the same grid stencil width is the same per method evaluation.

The new method is designed to perform well propagating small scale acoustic perturbations on a background compressible flow with shock waves. Future plans include applying the new method to problems that are more aeroacoustic in character, for example computation of vortex/shock interaction.

An issue not addressed here is boundary closure of DRP finite difference operators. Some results are available in [10]. However, this is a far from exhausted topic. A future research direction will be to investigate how the order of the SBP boundary approximation and the wave number ranges of the DRP optimization affect the accuracy and stability of the resulting acoustic wave computation.

Acknowledgment

Financial support from the NASA TTT/RCA program for the second author is gratefully acknowledged. The authors are grateful to Dr. Alan Wray of NASA Ames Research Center for the numerous valuable discussion throughout the course of this work.

References

[1] Arakawa A. Computational design for long-term numerical integration of the equations of fluid motion: two-dimensional incompressible flow, part i. J Comput Phys 1966;1:119–43.
[2] Blaisdell GA, Spyropoulos ET, Qin JH. The effect of the formulation of nonlinear terms on aliasing errors in spectral methods. Appl Num Math 1996;21:207–19.
[3] Bogey C, Bailly C. A family of low dispersive and low dissipative explicit excit schemes for computing the aerodynamic noise. In: Proceedings of the 8th ARAA/CEAS Aeroacoustics Conference & Exhibit, AIAA-paper 2002–2509,. Breckenridge Colorado; 2002. June 17–19
[4] Brachet M, Meiron D, Orszag S, Nickel B, Morf R, Frisch U. Small-scale structure of the Taylor-Green vortex. J Fluid Mech 1983;130:411.
[5] Brambley EJ. Optimized finite-difference (DRP) schemes perform poorly for decaying or growing oscillations. J Comput Phys 2015;324:258–74.
[6] Ducros F, Laporte F, Soulères T, Guinot V, Moinat P, Caruelle B. High-order fluxes for conservative skew-symmetric-like schemes in structured meshes: application to compressible flows. J Comput Phys 2000;161:114–39.
[7] Ducros F, Ferrand V, Nicoud F, Weber C, Darracq D, Gacherieu C, et al. Large-eddy simulation of the shock/turbulence interaction. J Comput Phys 1999;152:517–49.
[8] Haras Z, Taásan S. Finite difference schemes for long time integrations. J Comput Phys 1994;114:265.
[9] Harten A. The artificial compression method for computations of shocks and contact discontinuities: III. self-adjusting hybrid schemes. J Comput Phys 1978;32:363–89.
[10] Johansson S.. High order summation by parts operator based on a DRP scheme applied to 2D, Technical report2004-050. Sweden: Uppsala University.
[11] Kotov DV, Yee HC, Sjögreen B. Comparative study of high order positivity-preserving WENO schemes. In: Proceedings of the international conference on computational fluid dynamics ICCFD8. China: Chengdu, Sichuan; 2014. July 14–18
[12] Kotov DV, Yee HC, Panesi M, Prabhu DK, Wray AA. Computational challenges for simulations related to the NASA electric arc shock tube (EAST) experiments. J Comput Phys 2014;269:215–33.
[13] Kotov DV, Yee HC, Wray AA, Sjögreen B, Kritsuk AG. Numerical disipation control in high order shock-capturing schemes for LES of low speed flows. J Comput Phys 2016;307:189–202.
[14] Kotov DV, Yee HC, Wray AA, Sjögreen B. High order numerical methods for dynamic SGS model of turbulent flows with shocks. Commun Comput Phys 2016;19:273–300.
[15] Linders K, Nordström J. Uniformly best wavenumber approximations by spatial central difference operators. J Comput Phys 2015;300:695–709.
[16] Linders K, Kupiainen M, Nordström J. Summation-by-parts operators with minimal dispersion error for accurate and efficient flow calculations. In: Proceedings of the AIAA SciTech conference. San Diego; 2016. Jan. 4–8
[17] Lo SC, Blasisdell G, Lyrintzis A. High order shock capturing schemes for turbulence calculations. J Num Meth Fluids 2010;62:473.
[18] De Roeck W, Desmet W, Baelmans M, Sas P. An overview of high-order finite difference schemes for computational aeroacoustics. In: Proceedings of mechatronics and its applications ISMA 2004, September 20–22. Belgium: Katholieke Universiteit Leuven; 2004.
[19] Shu C-W, Osher SJ. Efficient implementation of essentially non-oscillatory shock capturing schemes. J Comput Phys 1989;83:32–78.
[20] Sjögreen B, Yee HC. Multiresolution wavelet based adaptive numerical dissipation control for high order methods. J Sci Comput 2004;20:211–55.
[21] Sjögreen B, Yee HC. On skew-symmetric splitting and entropy conservation schemes for the euler equations. In: Proceedings of the european conference on numerical mathematics and advanced applications, ENUMATH, 09, June 29-July 2. Sweden: Uppsala University; 2009.
[22] Sjögreen B, Yee HC. Skew-symmetric splitting and stability of high order central schemes. Proceeding of international conference on numerical modeling of

space plasma flows ASTRONUM-2016, June 6–10. CA, USA: Monterey; 2016. To appear
[23] Sjögreen B, Yee HC. Improving numerical stability via skew-symmetric splitting in multiscale gas dynamics and MHD turbulence flows. Extended version of the Proceeding of international conference on numerical modeling of space plasma flows ASTRONUM-2016, June 6–10. CA, USA: Monterey; 2017. Submitted to J. Comput. Phys., under journal review
[24] Sjögreen B, Yee HC. On high order entropy conserving numerical flux for multiscale gas dynamics and MHD turbulent simulations. Proceeding of international conference on Spectral and high order methods ICOSAHOM-2016, June 27-July 1. Brazil: Rio de Janeiro; 2016.
[25] Sjögreen B, Yee HC. Construction of high order entropy conserving numerical flux for multiscale gas dynamics and MHD turbulent simulations. Extended version of the Proceeding of international conference on spectral and high order methods ICOSAHOM-2016, June 27-July 1. Brazil: Rio de Janeiro; 2016. Submitted to J. Comput. Phys., 2016
[26] Sandham ND, Li Q, Yee HC. Entropy splitting for high-order numerical simulation of compressible turbulence. J Comput Phys 2002;23:307–22.
[27] Tam CKW. A CAA primer for practicing engineers. Proceeding of arnold engineering development center, AEDC-TR-08-2,. Tennssee: Arnold Air Force Base; 2008.
[28] Tam CKW. Computational aeroacoustics: a wave number approach. Cambridge Aerospace series. New York: Cambridge University Press; 2012. Vol. 33
[29] Taylor G, Green A. Mechanism of the production of small eddies from large ones. Proc. R. Soc. Lond. A. 1937;158:499.
[30] Tauber E, Sandham ND. Comparison of three large-eddy simulations of shock--induced turbulent separation bubbles. Shock Waves 2009;19:469–78.
[31] Yee HC, Sjögreen B. Development of low dissipative high order filter schemes for multiscale Navier–Stokes MHD systems. J Comput Phys 2007;225:910–34.
[32] Yee HC, Sjögreen B. High order filter methods for wide range of compressible flow speeds. In: Proceedings of the Proceeding of international conference on spectral and high order methods ICOSAHOM09, June 22–26. Norway: Trondheim; 2009.
[33] Yee HC, Sjögreen B. Adaptive filtering and limiting in compact high order methods for multiscale gas dynamics and MHD systems. Comput Fluids 2008;37:593–619.
[34] Yee HC, Sjögreen B. Efficient low dissipative high order schemes for multiscale MHD flows, II: minimization of $\nabla \cdot b$ numerical error. J Sci Comput 2006;29:115–64.
[35] Yee HC, Vinokur M, Djomehri MJ. Entropy splitting and numerical dissipation. J Comput Phys 2000;162:33–81.
[36] Yee HC, Sandham ND, Djomehri MJ. Low-dissipative high order shock--capturing methods using characteristic-based filters. J Comput Phys 1999;150:199–238.
[37] Yee HC, Klopfer GH, Montangne J-L. High-resolution shock-capturing schemes for inviscid and viscous hypersonic flows. J Comput Phys 1990;88:31–61.